Q-Ball Imaging

David S. Tuch[1,2]*

Magnetic resonance diffusion tensor imaging (DTI) provides a powerful tool for mapping neural histoarchitecture in vivo. However, DTI can only resolve a single fiber orientation within each imaging voxel due to the constraints of the tensor model. For example, DTI cannot resolve fibers crossing, bending, or twisting within an individual voxel. Intravoxel fiber crossing can be resolved using *q*-space diffusion imaging, but *q*-space imaging requires large pulsed field gradients and time-intensive sampling. It is also possible to resolve intravoxel fiber crossing using mixture model decomposition of the high angular resolution diffusion imaging (HARDI) signal, but mixture modeling requires a model of the underlying diffusion process.

Recently, it has been shown that the HARDI signal can be reconstructed model-independently using a spherical tomographic inversion called the Funk–Radon transform, also known as the spherical Radon transform. The resulting imaging method, termed *q*-ball imaging, can resolve multiple intravoxel fiber orientations and does not require any assumptions on the diffusion process such as Gaussianity or multi-Gaussianity. The present paper reviews the theory of *q*-ball imaging and describes a simple linear matrix formulation for the *q*-ball reconstruction based on spherical radial basis function interpolation. Open aspects of the *q*-ball reconstruction algorithm are discussed. Magn Reson Med 52:1358–1372, 2004. © 2004 Wiley-Liss, Inc.

Key words: diffusion MRI; diffusion tensor imaging; high angular resolution diffusion imaging; tractography

Magnetic resonance diffusion tensor imaging (DTI) maps the orientational architecture of neural tissue by measuring the water diffusion tensor within each voxel of the MR image (1–3). The orientational architecture of the underlying tissue can be inferred from the eigenstructure of the diffusion tensor. For example, the major eigenvector of the diffusion tensor gives the mean fiber direction within the voxel, and the minor eigenvector indicates the sheet normal vector (4). In cerebral white matter, the anisotropy of the diffusion tensor also provides a putative marker of myelination degree and fiber density (5,6).

DTI has a significant limitation, however, in that the technique can only resolve a single fiber direction within each voxel (7,8). This shortcoming is significant since human cerebral white matter possesses considerable intravoxel structure at the millimeter resolution typical of MRI. The tensor model is consequently deemed inadequate for

resolving neural architecture in regions with complex fiber patterns.

The inability of DTI to resolve intravoxel orientational heterogeneity has a number of consequences. This limitation presents a significant obstacle for efforts to trace white matter pathways from diffusion MRI (see Ref. (9) for review). The fiber crossing confound also complicates interpretation of diffusion anisotropy in regions of intravoxel heterogeneity. In cerebral white matter, the anisotropy of the diffusion tensor is typically expressed through the fractional anisotropy (FA) metric. In voxels containing intravoxel orientational heterogeneity, a *decrease* in the FA of an individual fiber population may result in a paradoxical *increase* in the overall FA (4,10).

DTI's inability to resolve intravoxel orientational heterogeneity stems from the constraints of the tensor model, which implicitly assumes a single Gaussian diffusion compartment within each voxel. The Gaussian function has only a single directional maximum and therefore cannot adequately describe diffusion functions with multiple maxima. Multimodal diffusion may arise when the fiber populations within a voxel possess different orientations and the diffusion between the populations is in slow exchange (7,8,11).

The fiber crossing confound in DTI has prompted efforts to develop diffusion imaging methods capable of resolving intravoxel fiber crossing (7,8,12–17). Using *q*-space imaging (QSI), investigators have measured the microscopic diffusion function directly and have found that in regions of fiber crossing the diffusion function possesses significant multimodal structure (12,14,18). QSI employs the Fourier relation between the diffusion signal and the diffusion function to measure the diffusion function directly, without recourse to a model of the diffusion process (19). QSI is also referred to as diffusion spectrum imaging (DSI) (12,14,18), diffusion displacement imaging, or dynamic NMR microscopy (19).

QSI measures the diffusion function directly by sampling the diffusion signal on a three-dimensional Cartesian lattice. The QSI technique suffers from two practical weaknesses however. The technique requires gradient sampling on a three-dimensional Cartesian lattice, which is time-intensive. Further, QSI requires large pulsed field gradients to satisfy the Nyquist condition for diffusion in nerve tissue.

To address the sampling burden of QSI, investigators have proposed an alternative approach based on sampling on a spherical shell (or combination of shells) in diffusion wavevector space. The spherical sampling approach referred to as high angular resolution diffusion imaging (HARDI) (8,11,15–17). In theory, the efficiency gain of HARDI would stem from the need to sample only on a spherical shell as opposed to the three-dimensional Cartesian volume required by QSI. By selecting a sampling shell

of a particular radius the acquisition could also be targeted toward specific lengthscales of interest.

Notwithstanding the potential advantages of HARDI, widespread application of the technique has been limited by the unavailability of a model-independent reconstruction scheme for HARDI data. Various models and numerical fitting procedures have been proposed to relate the spherical diffusion signal to the underlying diffusion function (7,8,15–17), but a model-free inversion has remained elusive.

Recently, we described a completely model-free reconstruction scheme for HARDI (12). The reconstruction is based on a spherical tomographic inversion called the Funk–Radon transform, also known as the spherical Radon transform or simply the Funk transform. The resulting method, called *q*-ball imaging (QBI), has a number of benefits over previous HARDI reconstruction approaches including model-independence, linearity in the signal, an image resolution framework, and computational simplicity. In the present paper we review the theoretical basis of the QBI method, provide a simple linear matrix formulation for the QBI reconstruction, and demonstrate the technique's ability to resolve intravoxel white matter fiber architecture.

THEORY

Background

In this section we review the theoretical relationship between the diffusion signal and the diffusion function. We then describe the theory for inversion of the diffusion signal using the Funk–Radon transform (FRT), which forms the basis of the QBI method.

The diffusion function can be described generally by the conditional diffusion probability density function $P(\mathbf{x},\mathbf{x}_0)$. The conditional probability density function describes the probability for a spin to displace from position $\mathbf{x}_0$ to position $\mathbf{x}$ in the experimental diffusion time τ (19–21). The conditional probability density function is referred to in other contexts as the diffusion Green's function, the diffusion propagator, or the diffusion van-Hove self-correlation function.

In MR, the observed signal is generated from an average over all spins in the voxel. The resulting ensemble-average is written $P(\mathbf{r}) = \int P(\mathbf{x},\mathbf{x}_0)\rho(\mathbf{x}_0)\,d\mathbf{x}_0$, where $\mathbf{r} = \mathbf{x} - \mathbf{x}_0$ is the relative spin displacement and $\rho(\mathbf{x}_0)$ is the initial spin density (19,21). With some abuse of nomenclature, we will refer to the ensemble average of the conditional probability density function as simply the probability density function (PDF) or diffusion function and denote it $P(\mathbf{r})$. In the notation that follows, the diffusion function $P(\mathbf{r})$ therefore denotes the ensemble-average probability for a spin to undergo a relative displacement $\mathbf{r}$ in the experimental diffusion time τ.

The diffusion PDF $P(\mathbf{r})$ is related to the measured MR diffusion signal by the Fourier relationship,

$$P(\mathbf{r}) = \mathscr{F}[E(\mathbf{q})],$$

where $\mathscr{F}$ denotes the Fourier transform with respect to the diffusion wavevector $\mathbf{q}$ (19–22). The diffusion wavevector

is defined as $\mathbf{q} = (2\pi)^{-1}\gamma\delta\mathbf{g}$, where γ is the gyromagnetic ratio for the nucleus of interest, δ is the diffusion gradient duration, and $\mathbf{g}$ is the diffusion gradient vector. The diffusion wavevector $\mathbf{q}$ is the reciprocal vector to the relative spin displacement vector $\mathbf{r}$.

The Fourier relation between the diffusion function and MR diffusion signal enables direct reconstruction of the diffusion function by Fourier transformation of a three-dimensional lattice sampling of *q*-space. Reconstruction of the diffusion PDF by Fourier transform of the diffusion signal forms the basis of the QSI method (19). QSI has been employed to measure the diffusion PDF in nonbiological materials with complex microstructure (19,23), as well as small animals in vivo (14,24–26). QSI has also been applied in humans to map the one-dimensional (27,28) and three-dimensional PDF (12,18).

In in vivo applications, reconstructing the diffusion PDF using the complex Fourier transform is not feasible since the phase of the signal is corrupted by biological motion, primarily due to cardiac pulsation. Instead, the diffusion function can be reconstructed using the modulus Fourier transform $P(\mathbf{r}) = \mathscr{F}[|E(\mathbf{q})|]$. Using the modulus FT as opposed to the full complex FT does not sacrifice any information since the diffusion signal is real and positive. The reality and positivity of the diffusion signal entails that the modulus FT and complex FT of the diffusion signal are equivalent. The reality of the diffusion signal follows from the symmetry of the diffusion propagator, and the positivity, which is not trivial, is a consequence of the positive definiteness of the diffusion propagator (18).

It should be noted that Fourier transformation of the diffusion signal only gives the diffusion PDF exactly when there is no appreciable diffusion during the diffusing encoding period. This condition requires that the diffusion mixing length associated with the diffusion encoding time is smaller than a characteristic diffusion restriction size of the material. The requirement for short diffusion pulses is referred to as the "narrow-pulse condition" (29). It has been shown that when the pulse duration is finite the resulting PDF can be described as a center-of-mass propagator, which is a spatially contracted form of the true PDF (29).

While the three-dimensional PDF provides invaluable information on the tissue microstructure, for the purposes of mapping the orientational architecture of tissue the primary object of interest is the orientational structure of the diffusion function. The orientational structure of the diffusion function can be described through the diffusion orientation distribution function (ODF). The diffusion ODF $\psi(\mathbf{u})$ is defined as the radial projection of the diffusion function,

$$\psi(\mathbf{u}) = \frac{1}{Z}\int_0^\infty P(r\mathbf{u})dr, \qquad [1]$$

where Z is a dimensionless normalization constant. The ODF framework is widely used in materials science to describe the orientational composition of polymers, liquid crystals, and grain composites (30,31).

The normalization constant in Eq. [1] ensures that the ODF is properly normalized to unit mass. Even though the

PDF is normalized, the ODF obtained by radial projection is not guaranteed to be normalized since the ODF is a distribution on the radial projections and not on the true sphere. To define the ODF over the proper sphere would require an integral over solid angle elements.

Using Eq. [1] we can derive the ODF for Gaussian diffusion. The PDF for anisotropic Gaussian diffusion is

$$P(\mathbf{r}) = (4\pi\tau)^{-3/2}|\mathbf{D}|^{-1/2}\exp(-\mathbf{r}^T\mathbf{D}^{-1}\mathbf{r}/(4\tau)),$$

where $|.|$ is the determinant. Integrating over radius as described by Eq. [1] gives the ODF,

$$\psi(\mathbf{u}) = \frac{1}{Z}\sqrt{\frac{\pi\tau}{\mathbf{u}^T\mathbf{D}^{-1}\mathbf{u}}}, \qquad [2]$$

where Z is a normalization constant.

The ODF can be derived from the diffusion PDF measured by QSI. Deriving the ODF from QSI has a number of limitations, however. Extracting the ODF from the PDF requires explicitly calculating the radial projection. The mapping between Cartesian and spherical coordinates systems may introduce Cartesian artifacts in the ODF. Cartesian coloration of the ODF may be a particular problem at the coarse Cartesian resolution typically used for QSI. Further, the radial projection is highly inefficient since the projection discards a considerable fraction of the acquired data. The efficiency of QSI is also hampered by the strong pulsed field gradients needed to satisfy the Nyquist condition for the diffusion PDF in cerebral white matter.

It is substantially more efficient to measure the diffusion ODF by directly sampling the diffusion signal on a spherical shell in diffusion reciprocal space. This approach forms the basis of QBI (12). Reconstructing the ODF directly using spherical sampling and reconstruction has a number of advantages. First, both the sampling and the reconstruction are both performed on the sphere so the reconstruction is immune to Cartesian reconstruction bias. With a spherical sampling scheme, there is also a natural framework for calculating the angular resolution, whereas it is not clear how to define the angular resolution for a Cartesian scheme. Last, the acquisition can be targeted to specific spatial frequency bands of interest by specifying the radius of the sampling shell. In the next section we review the theory underlying the QBI reconstruction.

Reconstruction

The QBI reconstruction is based on the FRT, also known as the spherical Radon transform or simply the Funk transform (32). The FRT is an extension of the planar Radon transform to the sphere. The FRT is a transform from the sphere to the sphere. Given a function on the sphere $f(\mathbf{w})$, where $\mathbf{w}$ is a unit direction vector, the FRT is defined as the sum over the corresponding equator, i.e., the set of points perpendicular to $\mathbf{w}$. The FRT $\mathcal{G}$ for a direction $\mathbf{u}$ can be written

$$\mathcal{G}[f(\mathbf{w})](\mathbf{u}) = \int_{\mathbf{w}\in\mathbf{u}^\perp} f(\mathbf{w})d\mathbf{w}$$

$$= \int f(\mathbf{w})\delta(\mathbf{w}^T\mathbf{u})d\mathbf{w},$$

where δ is the Dirac delta function.

While the original FRT is defined as a transform from the sphere to the sphere, here we extend the definition of the FRT to map from three-dimensional Cartesian space to the sphere. The extended FRT is defined as the FRT evaluated at a particular radius r'. Given a three-dimensional function $f(\mathbf{x})$, where $\mathbf{x}$ is a three-dimensional vector, the FRT at a particular radius r' is written

$$\mathcal{G}[f(\mathbf{x})](\mathbf{u}, r') = \int f(\mathbf{x})\delta(\mathbf{x}^T\mathbf{u})\delta(|\mathbf{x}| - r')d\mathbf{x}.$$

For notational simplicity we denote the above transform as simply $\mathcal{G}_{r'}$. In general, we also denote transforms $F[f(x)](y)$ as simply $F[f(x)]$ where the final argument is implied.

Recently, we have shown that the FRT of the diffusion signal gives a strong approximation to the ODF, that is,

$$\psi(\mathbf{u}) \approx \frac{1}{Z}\mathcal{G}_{q'}[E(\mathbf{q})], \qquad [3]$$

where q' is the radius of the sampling shell and Z is a normalization constant (12). This remarkable relationship entails that the sum of the diffusion signal over an equator approximately gives the diffusion probability in the direction normal to the plane of the equator. Consequently, to estimate the diffusion probability in a particular direction all that is needed is to sum the diffusion signal along the equator around that direction. This provides a model-free approach for estimating the diffusion probability from the spherically sampled diffusion signal (12).

We note that FRT of the diffusion signal has been described previously by Zavada and colleagues in the context of isotropic diffusion (33). We also note that the FRT bears a strong resemblance to the infinite anisotropy inversion model described by Behrens et al. (13). The latter has an additional constant term for the spherical fit. It may be possible to show that the two inversions are equivalent.

Equation [3] represents an approximation. The exact relationship between the ODF and the FRT can be written as follows. We write the PDF in cylindrical coordinates as $P(r,\theta,z)$. Without loss of generality, we take the z-axis to be along the direction of interest $\mathbf{u}$. In Appendix A we prove that the ODF and the FRT of the diffusion signal are related according to

$$\psi(\mathbf{u}) = \mathcal{G}_{q'}[E(\mathbf{q})]$$

$$= 2\pi q'\int P(r, \theta, z)J_0(2\pi q'r)rdr\, d\theta\, dz, \quad [4]$$

where J_0 is the zeroth-order Bessel function (12). This relationship states that the FRT of the diffusion signal gives the radial projection of the PDF, except that instead of the projection being along an infinitely thin line the projection is along a Bessel beam with a width defined by the width of the zeroth-order Bessel function (Fig. 1). The Bessel beam projection resembles the true radial projection to the extent that the mass of the zeroth-order Bessel function is concentrated at the origin.

FIG. 1. Schematic illustration of the relationship between the Funk–Radon transform and the Bessel beam projection. The q-space sampling scheme is indicated by the blue spherical lattice. The white arrow gives the direction of interest. The light blue circle indicates the equator around the direction of interest. Integration of the q-space signal along the equator defines a projection beam, which is shown by the dot pattern. The projection beam (i.e., Bessel beam) falls off in intensity according to the zeroth-order Bessel function. The intensity of the Bessel beam is indicated by the density of the green and yellow dots. The green dots indicate the positive signal contribution and the yellow dots the negative contribution.
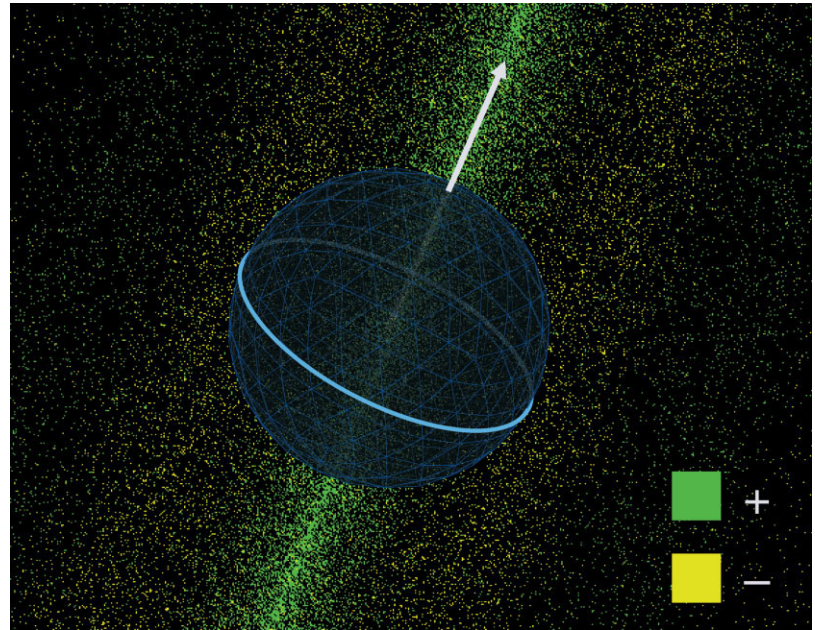
Equation [3] can be written in a simpler form by recalling the Hankel transform $\mathcal{H}[f(r,\theta,z)] = \int f(r,\theta,z)J_0(2\pi kr)r\,dr$ and the X-ray transform (also known as the planar Radon transform) $X[f(r,\theta,z)] = \int f(r,\theta,z)\,dz$. We then have

$$\psi(\mathbf{u}) = \mathcal{G}_{q'}[E(\mathbf{q})] = 2\pi q' \int \mathcal{H}[X[P]]d\theta.$$

The above relation states that the FRT of the diffusion signal is proportional to the Hankel transform of the X-ray transform of the diffusion function. Note that the X-ray transform evaluated at the origin is equivalent to the radial projection described by Eq. [1]. (It is important to note that the $2\pi q'$ term in Eq. [3] arises from the circle integral and so is equal to unity if the great circle sampling density is independent of the sampling wavevector q').

To understand Eq. [4] it is helpful to consider the integral in parts. The X-ray transform projects the diffusion function onto $r\theta$-plane, which is the tangent plane to the direction of interest z. Evaluating the X-ray transform at the origin $r = 0$ would give the radial projection exactly. Instead, the X-ray projection is multiplied by J_0 through the Hankel transform. The integral over the plane dr and
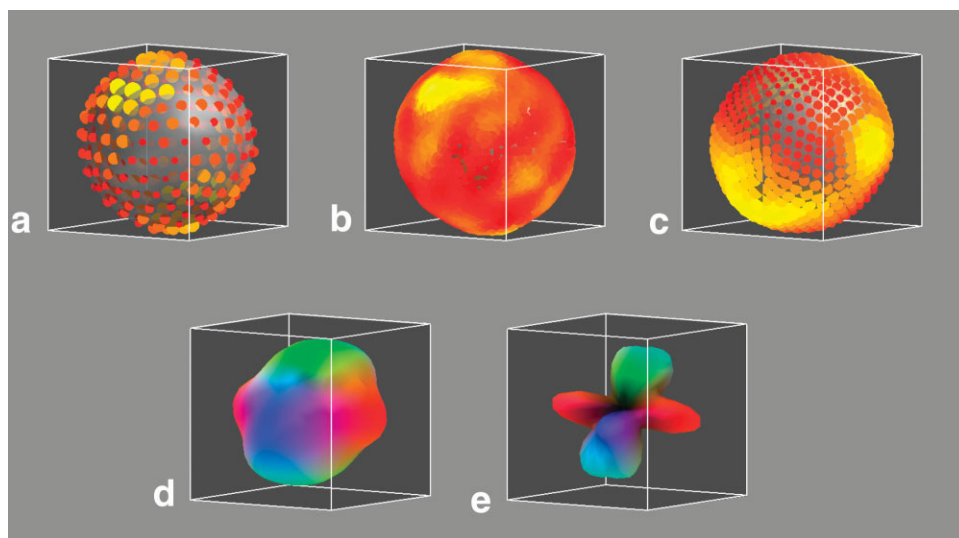

FIG. 2. Reconstruction of the diffusion ODF from the diffusion signal using the FRT. The diffusion data are taken from a single voxel from the data set described under Methods. The sampling and reconstruction schemes are also described under Methods. (a) Diffusion signal sampled on fivefold tessellated icosahedron ($m = 252$). The signal intensity is indicated by the size and color (white > yellow > red) of the dots on the sphere. (b) Regridding of diffusion signal onto set of equators around vertices of fivefold tessellated dodecahedron ($k \times n = 48 \times 755 = 36240$ points). (c) Diffusion ODF calculated using FRT. (d) Color-coded spherical polar plot rendering of ODF. (e) Min–max normalized ODF.

$d\theta$ then sums the weighted signal in the plane. To the extent that J_o is concentrated near the origin $r = 0$, Eq. [4] gives the true ODF. For example, for illustrative purposes, if we take $J_0(r) = \delta(r)$ then we obtain the true radial projection. The main consequence of Eq. [4] is that to estimate the diffusion probability in a particular direction we simply need to add the diffusion signal along the equator around that direction. Appendix A provides a detailed derivation of Eq. [4].

Implementing the FRT in practice requires a numerical procedure for calculating the equator integral. Since the equator points will not coincide with the diffusion wavevector sampling points it is necessary to regrid the diffusion data onto the equatorial circles. The regridding can be implemented using a form of spherical interpolation called spherical radial basis function (sRBF) interpolation, which we describe in the following section (34).

Algorithm

In this section we describe a simple matrix implementation of the FRT. We ultimately derive a matrix relationship of the form $\boldsymbol{\psi} = (1/Z)\,\mathbf{A}\mathbf{e}$ where the reconstruction matrix $\mathbf{A}$ implements the FRT. The following describes how to derive the FRT reconstruction matrix $\mathbf{A}$ and the normalization constant Z.

The diffusion signal for a diffusion wavevector q is denoted $E(\mathbf{q})$. We are given a set of m diffusion measurements, which we denote by the signal vector $\mathbf{e} = [E(\mathbf{q}_1)\ E(\mathbf{q}_2)\ \ldots\ E(\mathbf{q}_m)]^T$. The measurements were acquired with the m diffusion wavevectors $\{\mathbf{q}\} = \{\mathbf{q}_1, \mathbf{q}_2, \ldots, \mathbf{q}_m\}$. The diffusion wavevectors are also written as the $3 \times m$ column matrix $\mathbf{Q} = [\mathbf{q}_1\ \mathbf{q}_2 \ldots \mathbf{q}_m]$. For notational simplicity, the diffusion wavevectors are normalized to unit length, i.e., $\mathbf{q}_i \leftarrow \mathbf{q}_i/q$.

We specify a set of n diffusion directions of interest $\{\mathbf{u}\} = \{\mathbf{u}_1, \mathbf{u}_2, \ldots, \mathbf{u}_n\}$ onto which we wish to reconstruct the ODF. The reconstruction directions are also denoted by the $3 \times n$ column matrix $\mathbf{U} = [\mathbf{u}_1\ \mathbf{u}_2 \ldots \mathbf{u}_n]$. We wish to reconstruct the ODF vector $\boldsymbol{\psi} = [\psi(\mathbf{u}_1)\ \psi(\mathbf{u}_2)\ \ldots\ \psi(\mathbf{u}_n)]^T$ using the FRT.

To compute the FRT we need to specify the equator of points for each reconstruction direction $\mathbf{u}_i$. The points comprising each equator can be specified as follows. We construct a circle of k equally spaced points in the xy-plane. The points are denoted by the $3 \times k$ matrix $\mathbf{C} = [\cos\boldsymbol{\theta}\ \sin\boldsymbol{\theta}\ \mathbf{0}_k]^T$ where $\boldsymbol{\theta} = (2\pi/k)[1\quad 2 \ldots k]^T$ and $\mathbf{0}_k$ is a $k \times 1$ vector of zeros. For each $\mathbf{u}_i$, we then rotate the circle so that the normal to the circle-plane points in the direction $\mathbf{u}_i$. The rotation matrix is the matrix which rotates $\mathbf{z}$ into $\mathbf{u}_i$, which is given by

$$\mathbf{R}_{\mathbf{z}}(\mathbf{u}_i) = \frac{(\mathbf{z} + \mathbf{u}_i)(\mathbf{z} + \mathbf{u}_i)^T}{(\mathbf{z}^T\mathbf{u}_i + 1)} - \mathbf{I}.$$

The equator points for a $\mathbf{u}_i$ can then be written as $\mathbf{R}_{\mathbf{z}}(\mathbf{u}_i)\mathbf{C}$. We would like to represent all of the equator points for all of the reconstruction directions as a single matrix. To do so we form the $3 \times (kn)$ matrix $\mathbf{S} = \sqcap_{i=1}^{n} \mathbf{R}_{\mathbf{z}}(\mathbf{u}_i)\mathbf{C} = [\mathbf{R}_{\mathbf{z}}(\mathbf{u}_1)\mathbf{C}\ \mathbf{R}_{\mathbf{z}}(\mathbf{u}_2)\mathbf{C} \ldots \mathbf{R}_{\mathbf{z}}(\mathbf{u}_n)\mathbf{C}]$ where $\sqcap$ is the matrix concatenation operator.

The points on the equator do not correspond to sampling points so it is necessary to interpolate the data. We perform the interpolation by regridding the original sampling scheme onto the set of equators. The regridding is implemented using sRBF interpolation (34). The main idea of sRBF interpolation is to fit the signal with a linear combination of positive definite kernels on the sphere (35) and then use the kernel fit to evaluate the function at the interpolation points.

In order to implement the sRBF interpolation it is necessary to specify a basis function and a distance metric on the sphere. The distance metric d is taken to be the minimum angle between the direction vectors, i.e., $d(\mathbf{n}_1,\mathbf{n}_2) = \cos^{-1}|\mathbf{n}_1^T\mathbf{n}_2|$ where $\mathbf{n}_1$ and $\mathbf{n}_2$ are unit direction vectors, and $|.|$ denotes the absolute value. For the interpolation kernel we choose the spherical Gaussian $\phi(\alpha) = \exp(-\alpha^2/\sigma^2)$ where $\alpha = d(\mathbf{n}_1,\mathbf{n}_2)$ and σ is a width parameter. Other common basis functions for sRBF interpolation include the inverse multiquadric function $\phi(\alpha) = (\alpha^2 + \sigma^2)^{-1/2}$, thin-plate spline $\phi(\alpha) = \alpha^{2\sigma}\log(\alpha)$, and the ultraspherical (Gegenbauer) polynomial $\phi(\alpha) = C_n^\beta(\alpha)$ (34). Independent of sRBF interpolation, some other common basis functions for the ODF include the spherical harmonics (30) and the Wigner polynomials (36).

In sRBF interpolation the interpolation kernel width σ controls the tradeoff between the accuracy and the stability of the spherical interpolation; a small width will provide high accuracy but low stability and reciprocally for a large width. The accuracy–stability tradeoff is specified by the condition number of the interpolation matrix $\mathbf{H}$, so that the optimal tradeoff is achieved when the condition number is minimal (37). The optimal kernel width can be derived numerically knowing only the wavevector sampling scheme. It should also be possible to derive an analytical expression for the optimal kernel width (in a least upper-bounded sense) based on existing analytical upper bounds on the condition number of the spherical interpolation matrix (37).

The kernels are centered on a set of p specified unit vectors $\{\mathbf{v}\} = \{\mathbf{v}_1, \mathbf{v}_2, \ldots, \mathbf{v}_p\}$, which can be taken to be the sampling directions, the reconstruction points, or any other set of unit vectors. The basis function centers are also denoted by the $3 \times p$ column matrix $\mathbf{V} = [\mathbf{v}_1\ \mathbf{v}_2 \ldots \mathbf{v}_p]$. The diffusion signal can then be expressed as a convolution of the spherical basis functions, $\mathbf{e} = \mathbf{H}\mathbf{w}$, where $\mathbf{w}$ is the coefficient vector and $\mathbf{H}$ is the $m \times p$ convolution matrix $\mathbf{H} = [H_{ij}] = [\phi(d(\mathbf{q}_i, \mathbf{v}_j))] = \phi(\cos^{-1}|\mathbf{Q}^T\mathbf{V}|)$. From the measured signal $\mathbf{e}$ we can estimate the weight vector as $\hat{\mathbf{w}} = \mathbf{H}^+\mathbf{e}$ where $\mathbf{H}^+ = (\mathbf{H}^T\mathbf{H})^{-1}\mathbf{H}^T$ is the Moore–Penrose pseudoinverse of $\mathbf{H}$. If the noise is independent and identically distributed (iid) additive Gaussian noise, then noise regularization can be implemented using the noise-regularized pseudoinverse $\mathbf{H}^+ = (\mathbf{H}^T\boldsymbol{\Sigma}^{-1}\mathbf{H})^{-1}\mathbf{H}^T\boldsymbol{\Sigma}^{-1}$ where $\boldsymbol{\Sigma}$ is the noise covariance matrix for the signal vector $\mathbf{e}$.

The diffusion signal estimate for the equator points is given by $\mathbf{G}\mathbf{w}$ where $\mathbf{G} = [G_{ij}] = [\phi(d(\mathbf{s}_i, \mathbf{v}_j))] = \phi(\cos^{-1}|\mathbf{S}^T\mathbf{V}|)$ is the $(kn) \times p$ convolution matrix from the basis function centers to the equator points. Here, $\mathbf{s}_i$ and $\mathbf{v}_j$ are the column vectors of $\mathbf{S}$ and $\mathbf{V}$, respectively. Equating $\mathbf{w}$ and $\hat{\mathbf{w}}$ and substituting gives the $(kn) \times m$ matrix $\mathbf{G}\mathbf{H}^+$. To compute the sum over the equators, we define the summation matrix $\boldsymbol{\Xi} = (\mathbf{I}_n \otimes \mathbf{1}_k^T)$ where $\otimes$ is the matrix

Table 1
Summary of QBI Reconstruction Algorithm

Input
  $\mathbf{e}$: $m \times 1$ diffusion signal vector
  $\mathbf{Q}$: $3 \times m$ column matrix of diffusion sampling wavevectors
  $\mathbf{U}$: $3 \times n$ column matrix of reconstruction points
  $\mathbf{V}$: $3 \times p$ column matrix of basis function centers[a]
  k : Number of points on the equator[b]
  $\phi(\cdot)$: Spherical radial basis function
Output
  ψ : $n \times 1$ diffusion ODF vector
Algorithm
  $\mathbf{H} = \phi(\cos^{-1}|\mathbf{Q}^T\mathbf{V}|)$: Construct $m \times p$ convolution matrix
  $\boldsymbol{\theta} = (2\pi/k) [1 \quad 2 \dots k]^T$: Construct $k \times 1$ vector of angles
  $\mathbf{C} = [\cos\boldsymbol{\theta} \; \sin\boldsymbol{\theta} \; \mathbf{0}_k]^T$: Construct $3 \times k$ matrix of equator points in the *xy*-plane
  $\mathbf{S} = \Pi_{i=1}^n \mathbf{R_z}(\mathbf{u}_i)\mathbf{C}$: Construct $3 \times (kn)$ matrix of equator points for all points
  $\mathbf{G} = \phi(\cos^{-1}|\mathbf{S}^T\mathbf{V}|)$: Construct $(kn) \times p$ convolution matrix
  $\mathbf{A} = (\mathbf{I}_n \otimes \mathbf{1}_k^T)\mathbf{G}\mathbf{H}^+$: Form reconstruction matrix by summing over equator dimension[c]
  $Z = \mathbf{1}_n^T \mathbf{A}\mathbf{e}$: Calculate normalization constant
  $\psi = (1/Z)\,\mathbf{A}\mathbf{e}$: Compute ODF

[a]The basis function centers can be taken to be the reconstruction points, i.e., $\mathbf{V} = \mathbf{U}$.
[b]The number of equator points k can be selected so that $\mathbf{A}$ converges within a specified numerical accuracy, i.e., $\|\mathbf{A}(k+1) - \mathbf{A}(k)\|$ < numerical precision.
[c]It is not advised to actually form the summation matrix $(\mathbf{I}_n \otimes \mathbf{1}_k^T)$. Rather, the summation should be implemented by repartitioning the $(kn) \times m$ matrix $\mathbf{G}\mathbf{H}^+$ into a $k \times n \times m$ array and then summing over the first dimension.

direct product, $\mathbf{I}_n$ is the $n \times n$ identity matrix, and $\mathbf{1}_k$ is a $k \times 1$ vector of ones. The summation matrix can be written explicitly as

$$\boldsymbol{\Xi} = \begin{pmatrix} \mathbf{1}_k^T & & & \mathbf{0} \\ & \mathbf{1}_k^T & & \\ & & \ddots & \\ \mathbf{0} & & & \mathbf{1}_k^T \end{pmatrix}.$$

The operation of $\boldsymbol{\Xi}$ is to sum independently over each equator.

The ODF is then given by the summation over the equators $\psi = (1/Z)\,\boldsymbol{\Xi}\mathbf{G}\mathbf{H}^+\mathbf{e}$, or more simply $\psi = (1/Z)\,\mathbf{A}\mathbf{e}$, where we have defined $\mathbf{A} = \boldsymbol{\Xi}\mathbf{G}\mathbf{H}^+$ and $Z = \mathbf{1}_n^T\mathbf{A}\mathbf{e}$. The normalization constant Z ensures that the ODF, as a probability density, properly normalizes to unit mass. Table 1 summarizes the QBI reconstruction algorithm.

Figure 2 shows the reconstruction steps for an individual ODF. Note that the equatorial regridding (Fig. 2b) is not actually computed as part of the FRT reconstruction but is shown for illustrative purposes. The FRT reconstruction directly estimates the great circle integral without estimating the values on the great circle.

We note that the FRT reconstruction matrix $\mathbf{A}$ can be approximated using the simple relation $\mathbf{A} = \phi(\cos^{-1}|\mathbf{U}^T\mathbf{Q}|)$. We term this approximation the "soft equator" approximation. The reconstruction matrix for the soft equator approximation has the advantage of being considerably simpler to build than the full sRBF construction. The relationship between the soft equator approximation and the sRBF framework merits further investigation.

Depending on the application it can be helpful to smooth the reconstructed ODF. The ODF can be smoothed using a spherical convolution matrix. The choice of smoothing width should be motivated by the objectives of the particular study. For example, the kernel width can be selected to achieve a particular statistical distribution for the ODF; to improve orientational registration between subjects for group comparisons; or to facilitate visualization.

Resolution

The resolution of the QBI experiment is defined as the width of the Bessel beam. Since the resolution is defined in terms of the width of the Bessel beam, the resolution has dimensions length and not angle. According to the Rayleigh resolution criterion (38), the spatial resolution of the Bessel beam is defined as radial distance to the first crossing of the Bessel function. This gives a resolution $\Delta r = \alpha_0/(2\pi q') = 0.383/q'$ where $\alpha_0 = 2.405$ is the first zero crossing of J_0, i.e., $J_0(\alpha_0) = 0$.

The reciprocal relationship between the mass and the sharpness of the Bessel beam defines the tradeoff between signal-to-noise and angular resolution in QBI. For large q' the signal will be low, but the beam will be narrow and consequently the resolution will be high. Reciprocally, for small q' the signal will be high, but the beam will be wide and so the resolution will be low.

Postprocessing

Resolving intravoxel fiber crossing with QBI requires higher diffusion weighting than is typically employed in DTI. The high diffusion weighting raises a number of postprocessing considerations, which are not factors in DTI. In particular, the individual diffusion-weighted images have negligible anatomic contrast so that it is impossible to perform any intensity-based image correction such as Eddy-current correction, motion correction, or cardiac-pulsation artifact rejection. Motion correction is a particular concern given the long acquisition times required for QBI.

To generate sufficient contrast to perform motion correction and Eddy-current correction it should be possible to average the data in blocks and then perform the correction procedure on the averaged blocks. For example, the diffusion data could be averaged in blocks of n images, and then the motion correction and Eddy-current correction could then be performed on the averaged blocks. The blocking approach would require that the diffusion directions are sampled in proximal order.

Motion correction could also be implemented by acquiring T_2 images interspersed with the diffusion images. Motion correction could be performed on the T_2 images and the motion correction transform could then be applied to the intermediate diffusion-weighted images. The frequency of the T_2 acquisitions would control the robustness to large motions.

The inability to detect images corrupted by cardiac pulsation argues for the need for cardiac gating in high *b*-value
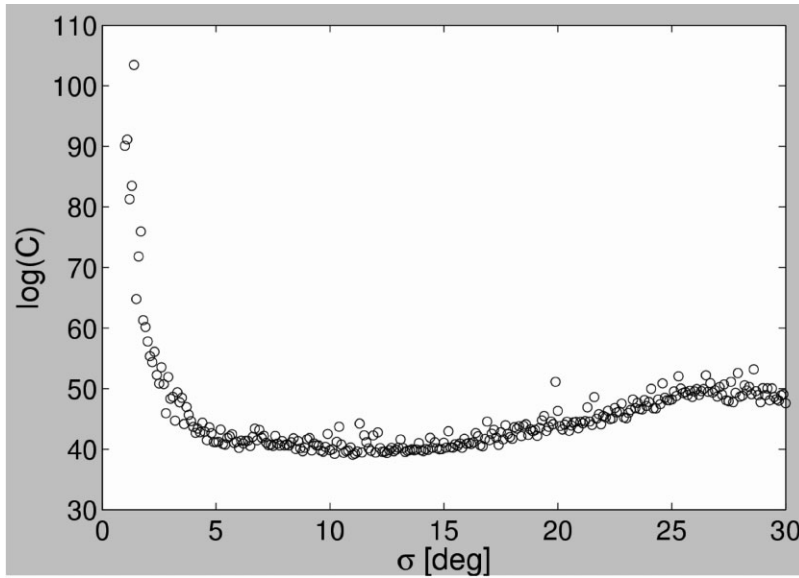
FIG. 3. Log condition number of the interpolation matrix **H** as a function of the kernel width σ.

diffusion imaging. The effect of the variable TR on the QBI reconstruction at low SNR would need to be investigated. It should be noted that none of the above procedures was used in the present study but will be investigated in future work.

Visualization

Visualization of ODF fields presents a number of challenges. The ODF can be visualized directly as a spherical polar plot $r(\mathbf{u}) = \psi(\mathbf{u})$. The diffusion peaks of the ODF are typically small though relative to the baseline (Fig. 2d) and so direct visualization of the ODF will show little orientational structure. To emphasize the orientational structure of the ODF, it is helpful to min–max normalize the ODF, i.e., subtract the baseline and rescale (Fig. 2e). By subtracting off the baseline term, however, the min–max normalization scales the noise nonlinearly potentially causing isotropic diffusion to appear anisotropic. For example, in the case of free diffusion with noise, the min–max normalization will produce noise peaks with high apparent anisotropy.

Rescaling the min–max normalized ODF by an anisotropy measure, e.g., the generalized fractional anisotropy (GFA) metric (Appendix B), resolves this confound by reintroducing the anisotropy information. The final spherical polar plot representation (Fig. 2c) is then

$$r(\mathbf{u}) = \mathrm{GFA}(\psi) \frac{\psi(\mathbf{u}) - \min \psi(\mathbf{u})}{\max \psi(\mathbf{u}) - \min \psi(\mathbf{u})}. \qquad [5]$$

Despite the ability of the anisotropy recalling to suppress the noise amplification, care should still be taken in interpreting diffusion peaks in regions of low anisotropy. We note that this choice of scaling is ad hoc and further visualization schemes should be explored.

METHODS

Data Acquisition

High angular resolution diffusion imaging data were collected on a normal human volunteer on a 3-T Siemens Trio using an eight-channel phased array coil. The data were collected at the Martinos Center for Biomedical Imaging using a protocol approved by the Massachusetts General Hospital Internal Review Board. The diffusion preparation used a twice-refocused balanced echo sequence $90-g_1-180-g_2-g_3-180-g_4-$acq where the 180 pulse-pair was positioned to minimized Eddy-current-induced image distortions (39). Thirty slices were acquired along the axial plane. The field of view was 282×282 mm and the matrix size was 128×128 to give 2.2×2.2 mm in-plane resolution. The slice thickness was 2.2 mm.

The sequence parameters were TR/TE = 6400/120 msec, $b = 4000$ sec/mm^2, $g_{\max} = 25$ mT/m, $g_{\mathrm{effective}} = 22.2$ mT/m, $\delta = 55$ msec, $q = 525$ cm^{-1}. This gives a spatial resolution (Rayleigh definition) $\Delta r = 7.28$ μm. The diffusion gradient sampling scheme consisted of $m = 252$ directions, which were obtained from the vertices of a fivefold regularly tessellated icosahedron (icosa5) projected onto the sphere. One T_2 image with no diffusion weighting was also obtained for a total of 253 acquisitions. The total acquisition time was 26′59″. The SNR of the T_2 image was 11. The mean SNR of the diffusion-weighted images was 2.5 ± 0.2 where the SD was computed over the diffusion directions.

Reconstruction

For each voxel the diffusion ODF was reconstructed using the matrix FRT described under Theory, Algorithm. The sRBF interpolation was implemented using a spherical Gaussian kernel with $\sigma = 5°$. The $n = 755$ reconstruction points were taken from the vertices of a fivefold regularly tessellated dodecahedron (dodeca5) projected onto the sphere. The basis function centers were taken as the same set of points. Each ODF was then smoothed using a spherical Gaussian kernel with $\sigma = 3°$. The number of equator sampling points was set at $k = 48$.

The width of the Gaussian kernel ($\sigma = 5°$) was selected by numerically solving for the σ which minimized the condition number of the interpolation matrix (Fig. 3). The condition number exhibited a broad minimum from $\sigma \approx$
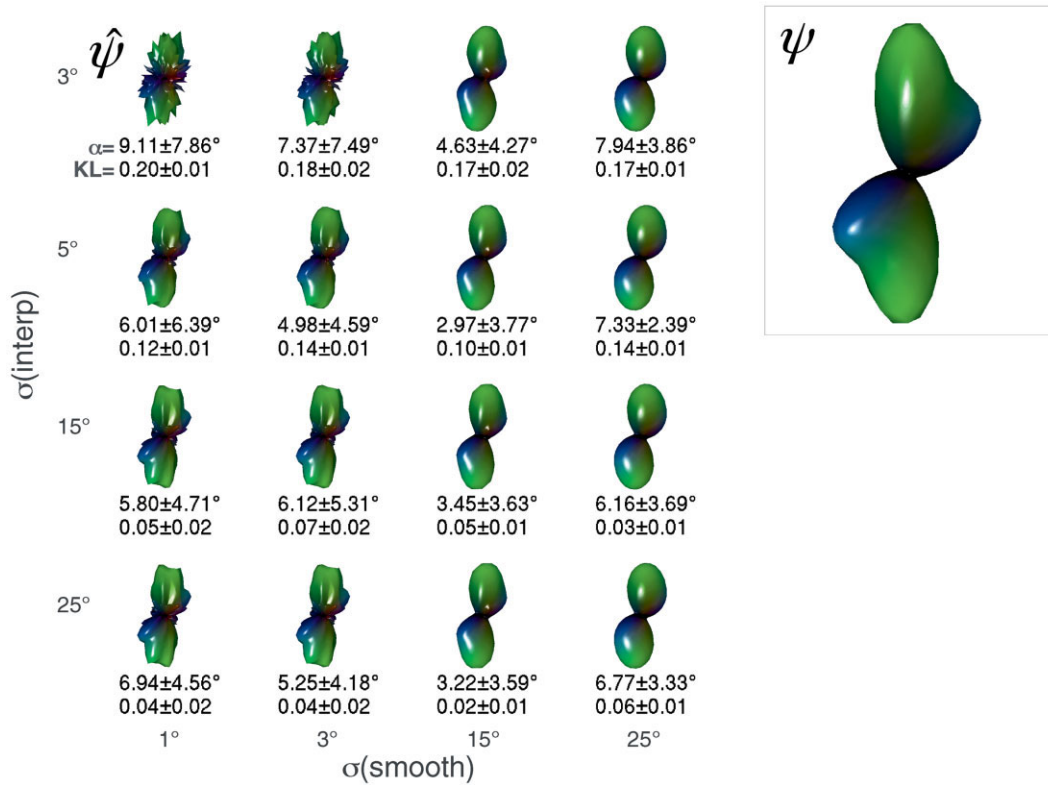
FIG. 4. Effect of smoothing and interpolation kernel widths on estimated ODF for a synthetic two-Gaussian system. The subplots show the estimated ODF $\hat{\psi}$ for an individual trial. The reconstruction was computed using the specified interpolation kernel width σ(interp) (rows) and smoothing kernel width σ(smooth) (columns). The error metrics below each ODF are the angular difference (top) and the KL divergence (bottom) between the true and estimated ODFs. The SD is the SD over trials. Note how the geometry of the reconstructed ODF is relatively constant for σ(interp) = {5,15,25}° for all levels of smoothing.

5–15°. The optimal σ was selected as the minimal value in this interval, $\sigma = 5°$. The width of the smoothing kernel ($\sigma = 3°$) was chosen by visual inspection of the min–max normalized ODFs in the genu of the corpus callosum and the crossings in prefrontal cortex. The width was selected with the goal of reducing sharp peaks in unimodal ODFs but not fusing peaks from multimodal ODFs.

Simulation

To assess the influence of the interpolation kernel width and the smoothing kernel width on the QBALL reconstruction we performed a numerical simulation of a two-compartment Gaussian system. The diffusion model consisted of two Gaussians in slow exchange. The volume fractions of the two compartments were $f_1 = 0.6$ and $f_2 = 0.4$. Each tensor had the same diffusion eigenvalues $\lambda = (1.7, 0.3, 0.3)\mu m^2/msec$. The principal eigenvectors were separated by 45°. The diffusion signal was sampled using the experimental parameters described above. The signal was sampled over $n = 100$ trials with Rician noise added to give SNR = 10 in the non-diffusion-attenuated signal. The true ODF was computed by analytical integration of the FRT.

The QBALL reconstruction was computed using a range of interpolation kernel widths σ(interp) = {3,5,15,25}° and smoothing kernel widths σ(smooth) = {1,3,15,25}°. The

reconstruction error between the estimated $\hat{\psi}$ and true ODF ψ was evaluated using two metrics: the mean angular difference between the maximum diffusion peak of the estimated and true ODFs; and the Kullback–Leibler (KL) divergence between the estimated and true ODFs. The angular difference metric was defined as $\alpha = \cos^{-1}|(\hat{\mathbf{u}}^*)^T \mathbf{u}^*|$ where $\hat{\mathbf{u}}^* = \arg\max_{\mathbf{u}} \hat{\psi}(\mathbf{u})$ and $\mathbf{u}^* = \arg\max_{\mathbf{u}} \psi(\mathbf{u})$. The KL divergence was defined as KL = $\sum_i \psi(\mathbf{u}_i)\log(\psi(\mathbf{u}_i)/\hat{\psi}(\mathbf{u}_i))$.

Figure 4 shows the effect of the interpolation kernel width and the smoothing kernel width on the ODF reconstruction for the simulated data. The angular difference metric is seen to decrease and then increase with increasing interpolation kernel width, which is consistent with the performance predicted by the condition number criterion (Fig. 3). Both the angular difference metric and the KL metric tended to decrease and then increase with increasing smoothing kernel width. The nonmonotonic behavior is due to the suppression of noise peaks at low smoothing levels and the fusion of true diffusion peaks at high smoothing levels.

RESULTS

General

Figure 5 shows the raw diffusion data for an individual slice and for a subset of the total number of diffusion
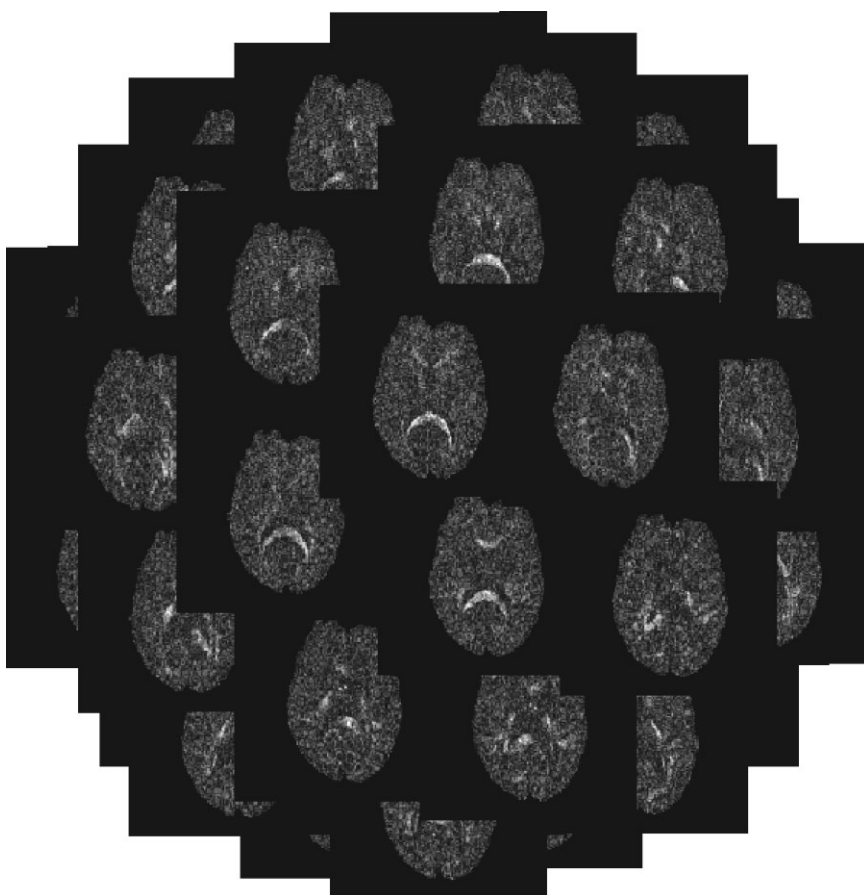
FIG. 5. Raw diffusion data for single slice and a subset of the total number of diffusion-weighted directions (42 of 252 diffusion directions). The images are arranged according to the corresponding sampling direction.

sampling directions. Anatomic contrast can only be seen in highly anisotropic structures such as the splenium of the corpus callosum. Figure 6 shows GFA and RGB maps for nine contiguous slices.

Optic Radiation

Figure 7 shows an ODF map of the optic radiation. The intersection among the optic radiation, the callosal splenium fibers, and the tapetum can be seen in the magnified inset (Fig. 7). The tapetum is a small group of association fibers medial to the optic radiation and lateral to the posterior horn of the lateral ventricle. The tapetum contains temporal–occipital association fibers (40), which run superior–inferiorly at the level of the splenium of the corpus callosum. The arcuate fasciculus can be seen on the lateral side of the optic radiation. The arcuate fasciculus originates from ventrolateral temporal gyri and the parietal and occipital lobes, sweeps superior and rostral around the insula, and inserts into the superior and middle frontal gyri.

The optic radiation fibers can be seen to diverge around the occipital sulcus to the middle and superior occipital gyri. At the cortical margin of the occipital sulcus intravoxel fiber crossings (green and red ODFs) are observed arising from the crossing between the anterior–posterior (green) directed fibers of the optic radiation and the medial–lateral (red) directed U-fibers connecting the middle and superior occipital gyri.

Meyer's Loop

Figure 8 shows an ODF map of the optic radiation including Meyer's loop. The optic radiation can be seen to originate in the lateral geniculate nucleus, arc over the inferior horn of the lateral ventricle, and travel medially to the arcuate fasciculus to insert into primary visual cortex. In Meyer's loop individual ODFs are observed with both anterior–posterior (green) and medial–lateral (red) directed peaks. The ability of a rapidly bending fiber population to generate ODFs with multiple peaks suggests that fiber crossing is not a prerequisite for multimodal ODFs. Rather, it may be possible for a single bending fiber population to generate multimodal ODFs.

The map also shows the intersection of the optic radiation and the uncinate fasciculus. The uncinate fasciculus connects the frontal lobe and the anterior temporal lobe. At the level of middle temporal lobe, the fibers of the uncinate fasciculus (blue) are joined by the anterior branch of the superior longitudinal fasciculus fibers (blue). In the middle temporal gyrus we see the lateral projections (red) to the gyral crown as well as anterior–posterior directed fibers (green) joining the middle temporal and superior temporal gyri.

Middle Temporal Gyrus

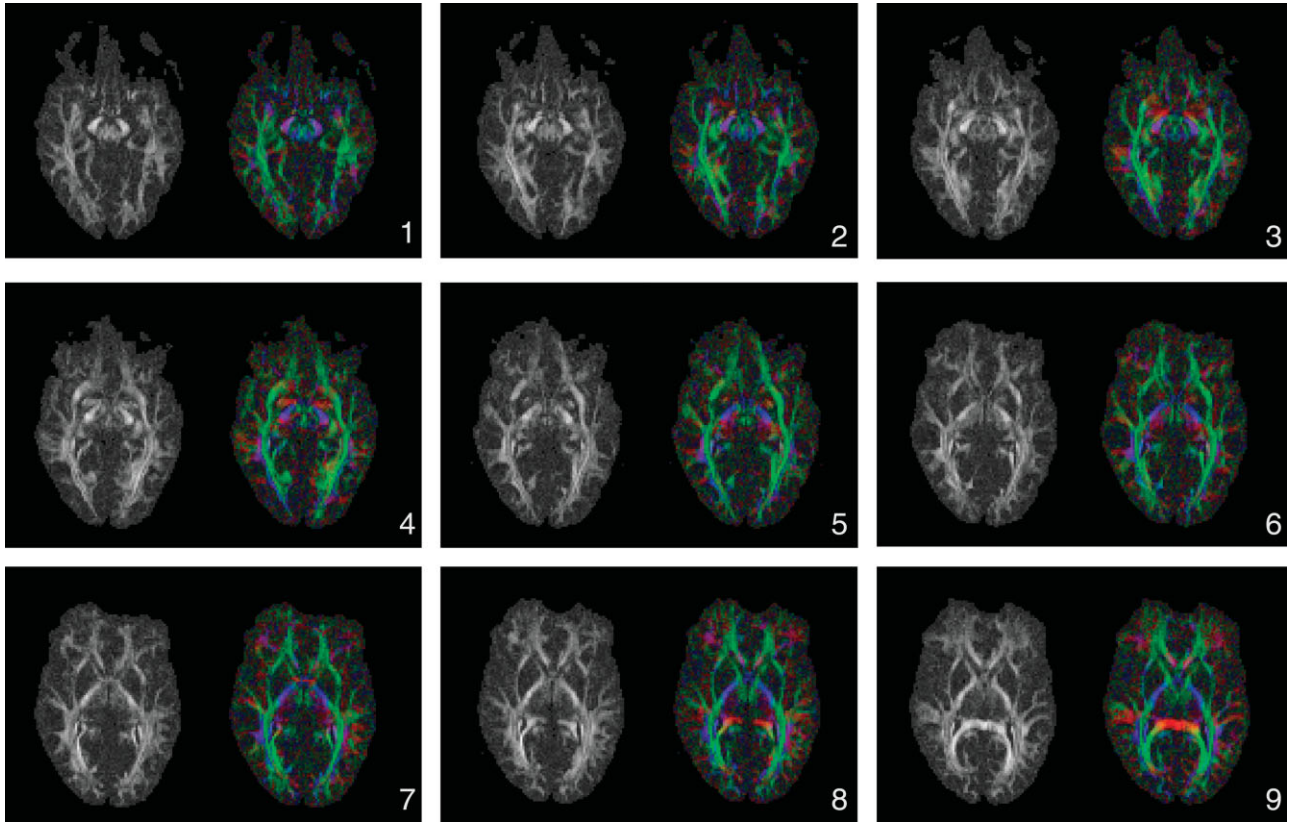The architecture of middle temporal gyrus is shown in detail in Fig. 9. Within the gyrus we see the lateral-

FIG. 6.   GFA and RGB images for nine slices. The slices are ordered inferior to superior in going from left to right and top to bottom. The RGB images are color-coded according to $(red, green, blue)^T = GFA \times |u^*|$ where $\mathbf{u}^*$ is the peak ODF direction, i.e., $\mathbf{u}^* = \arg\max_{\mathbf{u}} \psi(\mathbf{u})$. Red corresponds to medial–lateral, green anterior–posterior, and blue superior–inferior.

directed (red) projections along the gyral axis as well as fibers oriented anterior–posteriorly (green) perpendicular to the gyral axis. The anterior–posterior directed fibers may be the fiber component which inserts into the gyral wall or may be association fibers from superior temporal gyrus passing adjacent to the middle temporal gyrus on the way to the arcuate fasciculus.

FIG. 7.   ODF map of the intersection between the optic radiation and the splenium of the corpus callosum. The ODFs are rendered according to the scheme described in Theory, Visualization. The magnified view at right shows the crossing between splenium of the corpus callosum, the tapetum, and the optic radiation. af, arcuate fasciculus; mog, middle occipital gyrus; or, optic radiation; os, occipital sulcus; scc, splenium of the corpus callosum; sog, superior occipital gyrus; ta, tapetum.
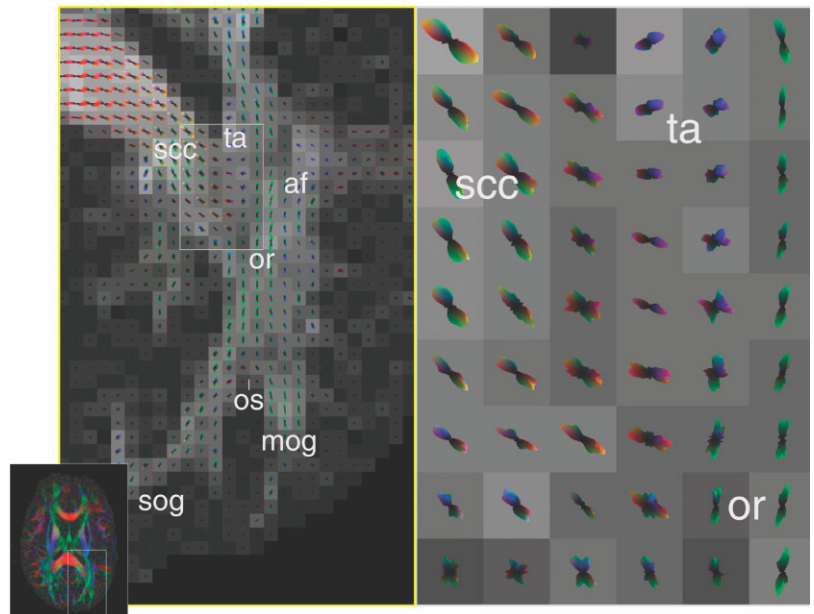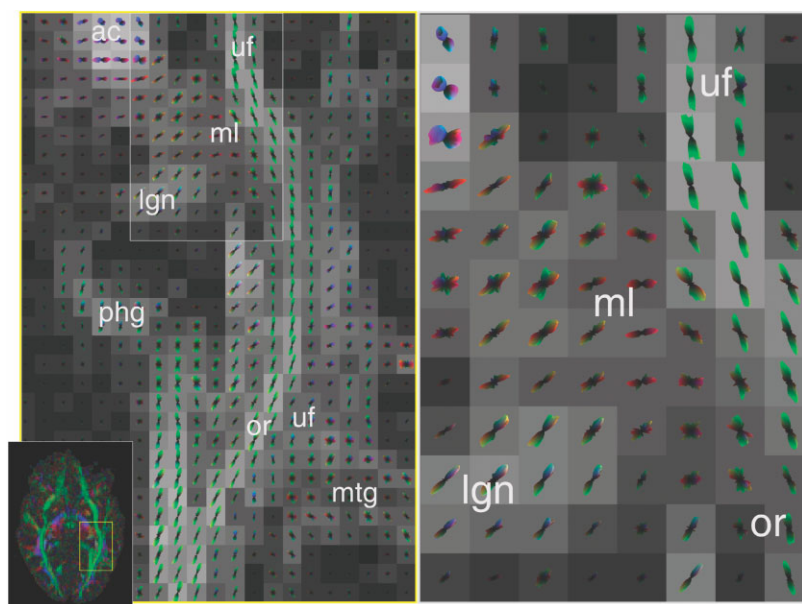
FIG. 8. ODF map of optic radiation and uncinate fasciculus. ac, anterior commisure.;lgn, lateral geniculate nucleus. The magnified view at right shows the apparent fiber crossing structure in Meyer's loop. ml, Meyer's loop; mtg, middle temporal gyrus; or, optic radiation; phg, parahippocampal gyrus; uf, uncinate fasciculus.

Midbrain

Figure 10 shows an ODF map of the caudal midbrain. The ODF map shows the decussation of the superior cerebellar peduncle (green turning into red) crossing the reticulospinal tract (blue), which runs superior–inferior. We also see the frontopotine fibers (green), which connect motor cortex and the pons, projecting anterior–posteriorly.

Prefrontal Cortex

The prefrontal cortical network is characterized by a complex interdigitation of thalamocortical and callosal projections (Fig. 11). Thalamocortical projections from the mediodorsal nucleus pass through the anterior limb of the internal capsule and diverge to insert into prefrontal cortex. The thalamocortical projections intersect callosal genu fibers, the superior longitudinal fasciculus, and fron-

tal association fibers. Multimodal ODFs are observed at the point where the thalamocortical projections diverge into the frontal gyri and where the projections intersect the callosal genu fibers.

Effect of Normalization

Figure 12 shows the effect of the various normalization steps (see Background, Visualization) on the rendered QBI (Fig. 12, top row) and DTI (Fig. 12, bottom row) ODF maps. In CSF, the unscaled ODFs obtained by QBI (Fig. 12a) are isotropic but the min–max normalized ODFs (Fig. 12b) exhibit artificial diffusion peaks due to the rescaling. It is important to note that the artificial peaks are not a result of anisotropy in the QBALL reconstruction, but are rather due to the nonlinear scaling of the noise peaks caused by the min–max normalization. Rescaling by GFA (Fig. 12c) suppresses the noise peaks in CSF yet retains the fiber
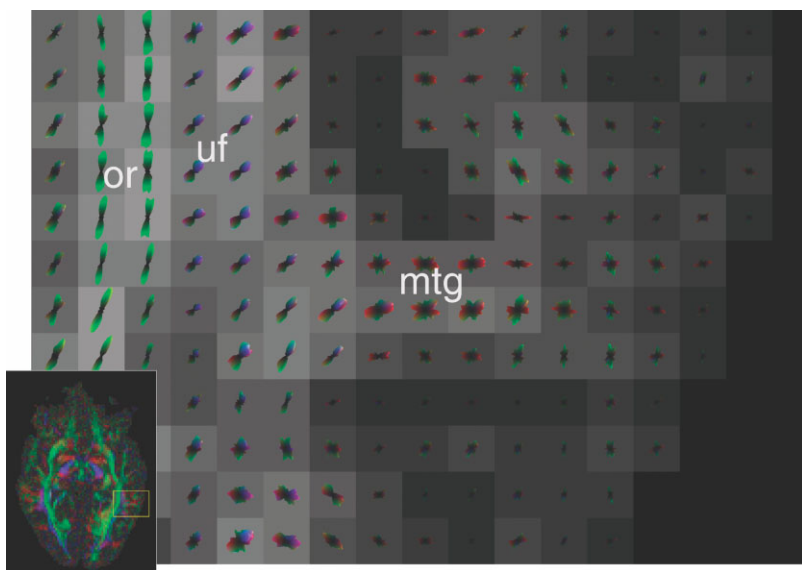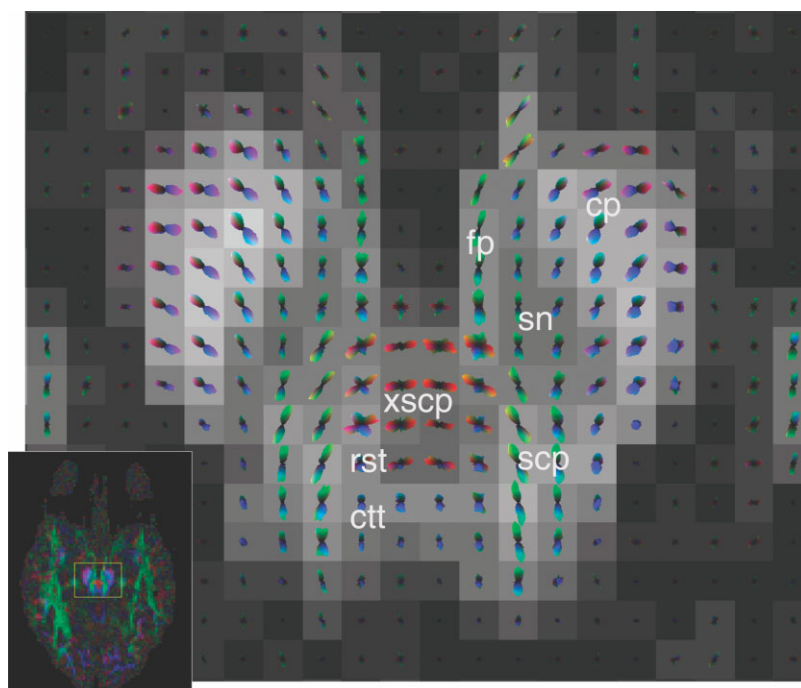

FIG. 9. ODF map of middle temporal gyrus, mtg, middle temporal gyrus; or, optic radiation; uf, uncinate fasciculus.

FIG. 10. ODF map of caudal midbrain. cp, cerebral peduncle; ctt, central tegmental tract; fp, frontopontine tract; rst, reticulospinal tract; scp, superior cerebellar peduncle; sn, substantia nigra; xscp, crossing of the superior cerebellar peduncle.

crossing contrast. For example, in the GFA-scaled, min–max normalized ODF map (Fig. 12c) fiber crossing can be seen at the crossing between the genu of the corpus callosum and anterior cingulate gyrus (white arrow) and at the bifurcation of the callosal genu fibers (white arrow).

Comparing Figs. 12c and 12e we see that QBI and DTI give similar ODF estimates in the core of the genu of the callosum. Note that the DTI and QBI ODFs will not be identical though, even for Gaussian diffusion because the

QBI ODF contains the Bessel term whereas the DTI ODF does not.

DISCUSSION

We have described a simple linear reconstruction scheme for QBI and shown that the technique can resolve intra-voxel fiber crossing both in deep white matter pathways and at the subcortical margin. Relative to DTI, the QBI

FIG. 11. ODF map of prefrontal cortex. acg, anterior cingular gyrus; gcc, genu of the corpus callosum; ic, internal capsule; ifg, inferior frontal gyrus; ec, external capsule; mfg; middle frontal gyrus; sfg, superior frontal gyrus.
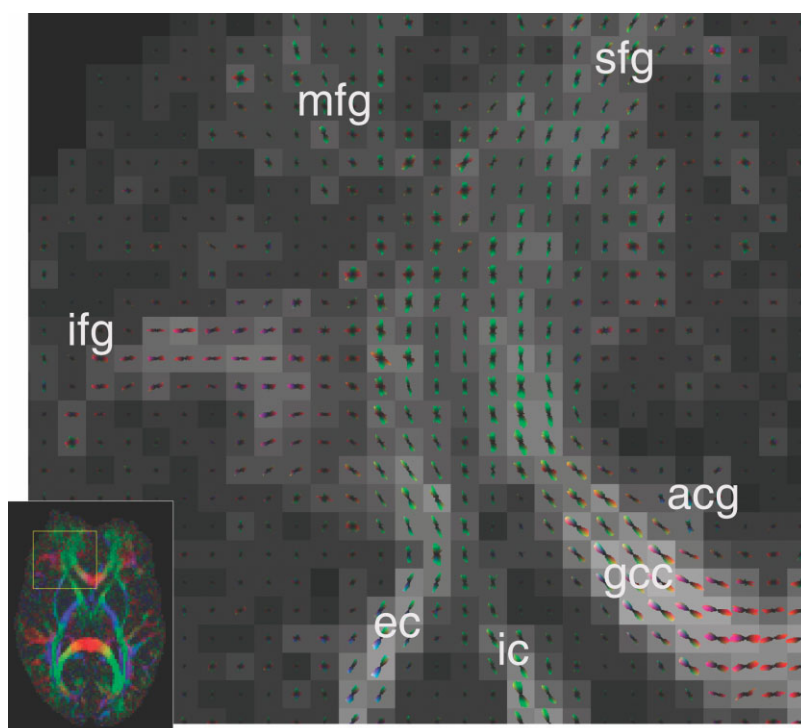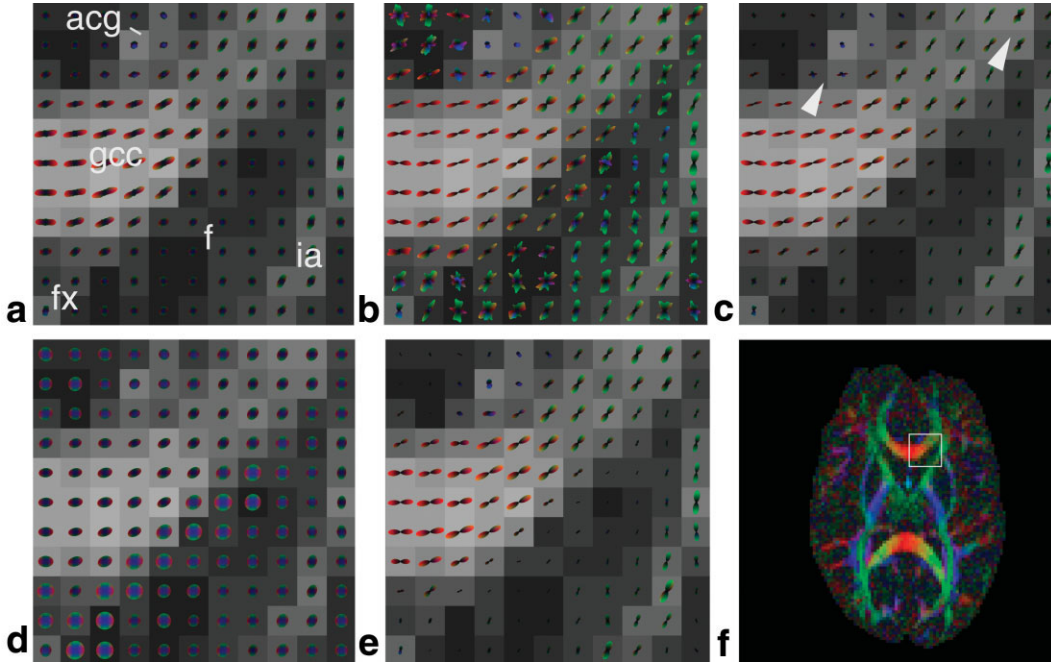
FIG. 12.   Effect of normalization on QBI (top row) and DTI (bottom row) ODF maps. The ROI is taken from the genu of the corpus callosum (ROI shown at bottom right). Frames (**a–c**) show QBI ODF maps where each ODF is (a) normalized to unit mass; (b) min–max normalized; (c) min–max normalized and then scaled by GFA as described by Eq. [5]. Note how the min–max normalized ODF map amplifies the noise in CSF. In the GFA-scaled, min–max normalized ODF map (c) fiber crossing can be seen at the crossing between gcc and acg (white arrow) and at the bifurcation of the projections from the gcc (white arrow). Frames (**d,e**) show the DTI ODF map where each ODF is (d) normalized to unit mass; (e) normalized to unit mass and then scaled by FA. The DTI ODF was derived from Eq. [2]. acg, anterior cingulate gyrus; f, frontal horn of lateral ventricle; fx, fornix; ia, anterior limb of internal callosum.

reconstruction has a number of advantages including linearity in the signal, model-independence, and the ability to resolve intravoxel orientational heterogeneity.

In regions containing intravoxel fiber curvature, such as Meyer's loop (Fig. 8), the reconstructed ODF may exhibit multiple peaks due the different directional components of the curving fiber bundle. In contrast, DTI would give a single diffusion peak, which arguably provides a more accurate representation of the number of fiber populations present. The ability of curving fibers to generate multimodal ODFs is a limitation of the ODF representation, which can describe multimodal diffusion but cannot resolve the continuity of an individual fiber orientation within a voxel. Care should therefore be taken in necessarily ascribing multimodal diffusion to fiber crossing as both crossing and bending fibers can give rise to multimodal diffusion. In particular, tractography algorithms, which do not consider the entire structure of the ODF but only the local diffusion peak, will be confounded by intravoxel fiber curvature.

It may be possible to differentiate bending from crossing fibers based on differences in the diffusion profiles for the two configurations. Toward that end, future research will investigate the effect of the diffusion wavevector and diffusion mixing and encoding times on the structure of the diffusion ODF in crossing and bending fiber populations.

APPENDIX A

Proof of the FRT–ODF Relationship

In Ref. (12). we provided a proof of the FRT–ODF relationship (Eq. [4]) using Plancheral's theorem and the central slice theorem. In this Appendix we derive a separate proof of the FRT–ODF relationship based on a cylindrical wave expansion.

Using cylindrical coordinates, the real space (diffusion space) vector is written as $\mathbf{r} = (r, \theta, z)$ and the Fourier space (diffusion signal space) vector is written $\mathbf{q} = (q, \vartheta, \zeta)$. Without loss of generality we take the direction of interest $\mathbf{u}$ to be the z-axis. The radial projection (Eqn. 1) can then be written as

$$p(r, \theta) = \int_{-\infty}^{+\infty} P(r, \theta, z)\,dz.$$

The FRT of E at wavevector q' is defined as the great circle integral

$$\mathcal{G}_{q'}[E] = \int E(q', \vartheta, 0)\,d\vartheta$$

$$= \int E(q, \vartheta, \zeta)\delta(q' - q)\delta(\zeta)q\,dq\,d\vartheta\,d\zeta.$$

Substituting the Fourier relation between E and P into the above equation gives

$$\mathcal{G}_{q'}[E] = \int P(r,\ \theta,\ z) e^{2\pi i[z\zeta + qr\cos(\theta - \vartheta)]} \delta\ (q' - q)$$

$$\times\ \delta(\zeta) q\ dq\ d\vartheta\ d\zeta\ r\ dr\ d\theta\ dz.$$

Integrating over z and ζ we obtain

$$\mathcal{G}_{q'}[E] = \int p(r,\ \theta) e^{2\pi i qr\cos(\theta - \vartheta)} \delta(q' - q) q\ dq\ d\vartheta\ r\ dr\ d\theta.$$

The exponential in the above equation can be expanded into cylindrical waves using the cylindrical wave expansion (i.e., Bessel function identity or Jacobi–Anger expansion),

$$e^{ix\cos\alpha} = \sum_{n=-\infty}^{+\infty} i^n J_n(x) e^{in\alpha}.$$

Integrating over q and ϑ we have

$$\mathcal{G}_{q'}[E] = q' \int \sum_{n=-\infty}^{+\infty} \frac{i}{n} e^{-(3/2)\pi ni + in\theta}$$

$$\times\ (1 - e^{2\pi ni}) p(r,\ \theta) J_n(2\pi q' r) r\ dr\ d\theta.$$

Since $(1 - e^{2\pi ni})/n = 0$ for all $n \neq 0$, only the $n = 0$ term contributes. Using

$$\lim_{n \to 0} (1 - e^{2\pi ni})/n = -2\pi i,$$

we finally obtain

$$\therefore \mathcal{G}_{q'}[E] = 2\pi q' \int p(r,\ \theta) J_0(2\pi q' r) r\ dr\ d\theta.$$

APPENDIX B

Scalar Measures

Scalar measures on the ODF are useful to define tissue contrast, perform statistical analyses, or summarize geometric properties of the ODF. We define the following scalar measures: GFA, entropy, and order.

As an extension of the FA metric which is defined as $FA = std(\lambda)/rms(\lambda)$ where λ are the eigenvalues of the diffusion tensor, we define the GFA

$$GFA = \frac{std(\psi)}{rms(\psi)}$$

$$= \sqrt{\frac{n \sum_{i=1}^{n} (\psi(\mathbf{u}_i) - \langle\psi\rangle)^2}{(n-1) \sum_{i=1}^{n} \psi(\mathbf{u}_i)^2}},$$

where $\langle\psi\rangle = (1/n) \sum_{i=1}^{n} \psi(\mathbf{u}_i) = (1/n)$ is the mean of the ODF. The last equality follows from the normalization of the ODF. Note that like the FA metric for DTI, the GFA metric is automatically normalized to [0,1]. We also define the normalized entropy

$$NE = -\frac{n}{\log n} \langle\log \psi\rangle$$

and the nematic order parameter (31)

$$S = \frac{1}{2} \langle 3 \cos^2 \mathbf{u}_i^T \langle\mathbf{u}\rangle - 1\rangle,$$

where $\langle\mathbf{u}\rangle$ is the mean diffusion direction, and $\langle.\rangle$ denotes the average over ψ.

REFERENCES

1. Le Bihan D. Looking into the functional architecture of the brain with diffusion MRI. Nat Rev Neurosci 2003;4:469−480.
2. Basser PJ, Mattiello J, LeBihan D. MR diffusion tensor spectroscopy and imaging. Biophys J 1994;66:259−267.
3. Pierpaoli C, Jezzard P, Basser PJ, Barnett A, Di Chiro G. Diffusion tensor MR imaging of the human brain. Radiology 1996;201:637−648.
4. Wiegell MR, Larsson HB, Wedeen VJ. Fiber crossing in human brain depicted with diffusion tensor MR imaging. Radiology 2000;217:897−903.
5. Norris DG. The effects of microscopic tissue parameters on the diffusion weighted magnetic resonance imaging experiment. NMR Biomed 2001;14:77−93.
6. Beaulieu C. The basis of anisotropic water diffusion in the nervous system—a technical review. NMR Biomed 2002;15:438−455.
7. Alexander AL, Hasan KM, Lazar M, Tsuruda JS, Parker DL. Analysis of partial volume effects in diffusion-tensor MRI. Magn Reson Med 2001; 45:770−780.
8. Tuch DS, Reese TG, Wiegell MR, Makris N, Belliveau JW, Wedeen VJ. High angular resolution diffusion imaging reveals intravoxel white matter fiber heterogeneity. Magn Reson Med 2002;48:577−582.
9. Mori S, Van Zijl PC. Fiber tracking: principles and strategies—a technical review. NMR Biomed 2002;15:468−480.
10. Pierpaoli C, Barnett A, Pajevic S, Chen R, Penix LR, Virta A, Basser P. Water diffusion changes in Wallerian degeneration and their dependence on white matter architecture. Neuroimage 2001;13:1174−1185.
11. Alexander DC, Barker GJ, Arridge SR. Detection and modeling of non-Gaussian apparent diffusion coefficient profiles in human brain data. Magn Reson Med 2002;48:331−340.
12. Tuch DS, Reese TG, Wiegell MR, Wedeen VJ. Diffusion MRI of complex neural architecture. Neuron 2003;40:885−895.
13. Behrens TE, Woolrich MW, Jenkinson M, Johansen-Berg H, Nunes RG, Clare S, Matthews PM, Brady JM, Smith SM. Characterization and propagation of uncertainty in diffusion-weighted MR imaging. Magn Reson Med 2003;50:1077−1088.
14. Lin CP, Wedeen VJ, Chen JH, Yao C, Tseng WY. Validation of diffusion spectrum magnetic resonance imaging with manganese-enhanced rat optic tracts and ex vivo phantoms. Neuroimage 2003;19:482−495.
15. Frank L. Anisotropy in high angular resolution diffusion-weighted MRI. Magn Reson Med 2001;45:935−939.

16. Ozarslan E, Mareci TH. Generalized diffusion tensor imaging and analytical relationships between diffusion tensor imaging and high angular resolution diffusion imaging. Magn Reson Med 2003;50:955–965.

17. Jansons KM, Alexander DC. Persistent angular structure: new insights from diffusion magnetic resonance imaging data. Inverse Problems 2003;19:1031–1046.

18. Tuch DS. Diffusion MRI of Complex Tissue Structure [Doctoral Dissertation]. Cambridge, Massachusetts: Harvard University–Massachusetts Institute of Technology; 2002. 218 p.

19. Callaghan PT. Principles of Nuclear Magnetic Resonance Microscopy. Oxford: Oxford University Press; 1993.

20. Stejskal EO, Tanner JE. Spin diffusion measurements: spin echoes in the presence of a time-dependent field gradient. J Chem Phys 1965;42: 288–292.

21. Kärger J, Heink W. The propagator representation of molecular transport in microporous crystallites. J Magn Reson 1983;51:1–7.

22. Cory DG, Garroway AN. Measurement of translational displacement probabilities by NMR: an indicator of compartmentation. Magn Reson Med 1990;14:435–444.

23. Callaghan PT. Rheo-NMR: nuclear magnetic resonance and the rheology of complex fluids. Rep Progress Phys 1999;62:500.

24. Assaf Y, Cohen Y. Structural information in neuronal tissue as revealed by q-space diffusion NMR spectroscopy of metabolites in bovine optic nerve. NMR Biomed 1999;12:335–344.

25. King MD, Houseman J, Gadian DG, Connelly A. Localized q-space imaging of the mouse brain. Magn Reson Med 1997;38:930–937.

26. King MD, Houseman J, Roussel SA, van Bruggen N, Williams SR, Gadian DG. q-Space imaging of the brain. Magn Reson Med 1994;32: 707–713.

27. Assaf Y, Ben-Bashat D, Chapman J, Peled S, Biton IE, Kafri M, Segev Y, Hendler T, Korczyn AD, Graif M, Cohen Y. High b-value q-space analyzed diffusion-weighted MRI: application to multiple sclerosis. Magn Reson Med 2002;47:115–126.

28. Cohen Y, Assaf Y. High b-value q-space analyzed diffusion-weighted MRS and MRI in neuronal tissues—a technical review. NMR Biomed 2002;15:516–542.

29. Mitra PP, Halperin BI. Effects of finite gradient-pulse widths in pulsed-field gradient diffusion measurements. J Magn Reson A 1995;113:94–101.

30. Kocks UF, Tomé CN, Wenk HR. Texture and anisotropy. Cambridge: Cambridge University Press; 2001.

31. de Gennes PG, Prost J. The Physics of Liquid Crystals. Oxford: Oxford University Press; 1995.

32. Funk P. Über eine geometrische Anwendung der Abelschen Integralgleichnung. Math Ann 1916;77:129–135.

33. Zavada T, Sudland N, Kimmich R, Nonnenmacher TF. Propagator representation of anomalous diffusion: the orientational structure factor formalism in NMR. Phys Rev E 1999;60:1292–1298.

34. Fasshauer GE, Schumaker LL. Scattered data fitting on the sphere. In: Daehlen M, Lyche T, Schumaker LL, editors. Mathematical Methods for Curves and Surfaces II, Innovations in Applied Mathematics. Nashville: Vanderbilt University Press; 1998. pp 117–166.

35. Schoenberg IJ. Positive definite functions on spheres. Duke Math J 1942;9:96–108.

36. Van Gurp M. The use of rotation matrices in the mathematical description of molecular orientations in polymers. Colloid Polym Sci 1995; 273:607–625.

37. Narcowich F, Sivakumar N, Ward JD. Stability results for scatter data interpolation on Euclidean spheres. Adv Comp Math 1998;8:137–163.

38. Rayleigh L. Investigations in optics with special reference to the spectroscope. Phil Mag 1879;8:261–274.

39. Reese TG, Heid O, Weisskoff RM, Wedeen VJ. Reduction of eddy-current-induced distortion in diffusion MRI using a twice-refocused spin echo. Magn Reson Med 2003;49:177–182.

40. Tusa RJ, Ungerleider LG. Fiber pathways of cortical areas mediating smooth pursuit eye movements in monkeys. Ann Neurol 1988;23:174–183.